



HAL
open science

PV-LVNet Direct left ventricle multitype indices estimation from 2D echocardiograms of paired apical views with deep neural networks

Rongjun Ge, Guanyu Yang, Yang Chen, Limin Luo, Cheng Feng, Heye Zhang,
Shuo Li

► **To cite this version:**

Rongjun Ge, Guanyu Yang, Yang Chen, Limin Luo, Cheng Feng, et al.. PV-LVNet Direct left ventricle multitype indices estimation from 2D echocardiograms of paired apical views with deep neural networks. *Medical Image Analysis*, 2019, 58, pp.101554. 10.1016/j.media.2019.101554. hal-02304385

HAL Id: hal-02304385

<https://univ-rennes.hal.science/hal-02304385v1>

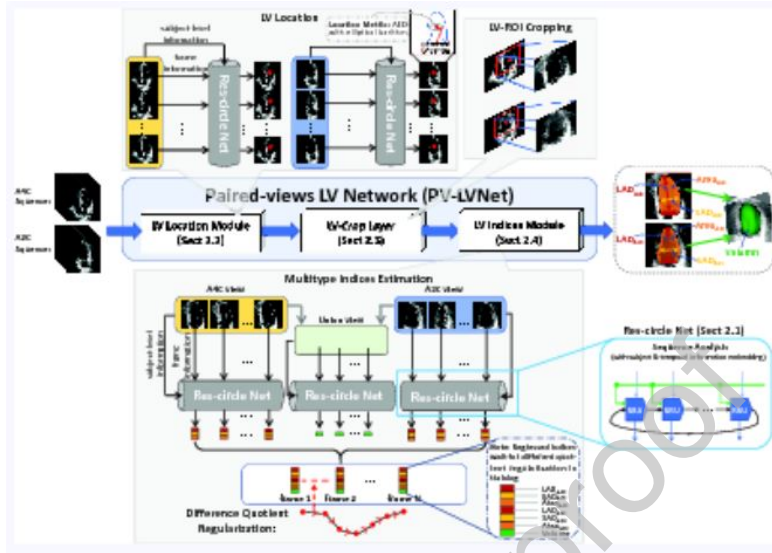
Submitted on 28 Nov 2019

HAL is a multi-disciplinary open access archive for the deposit and dissemination of scientific research documents, whether they are published or not. The documents may come from teaching and research institutions in France or abroad, or from public or private research centers.

L'archive ouverte pluridisciplinaire **HAL**, est destinée au dépôt et à la diffusion de documents scientifiques de niveau recherche, publiés ou non, émanant des établissements d'enseignement et de recherche français ou étrangers, des laboratoires publics ou privés.

Highlights

- An effective method for quantifying LV from multiple dimensions and views.
- A brand-new recurrent net for embedding subject and temporal information.
- An efficient location loss function for robust location and cropping.
- A creative regularization item for enhancing sequential data evolution fitting.



PV-LVNet: Direct Left Ventricle Multitype Indices Estimation from 2D Echocardiograms of Paired Apical Views with Deep Neural Networks

Rongjun Ge^{a,c,d}, Guanyu Yang^{a,c,d}, Yang Chen^{a,b,c,d,*}, Limin Luo^{a,c,d},
Cheng Feng^e, Heye Zhang^f, Shuo Li^{g,h,*}

^a*Laboratory of Image Science and Technology, School of Computer Science and Engineering, Southeast University, Nanjing, China*

^b*School of Cyber Science and Engineering, Southeast University, Nanjing, China*

^c*Key Laboratory of Computer Network and Information Integration (Southeast University), Ministry of Education, Nanjing, China*

^d*Centre de Recherche en Information Biomedicale Sino-Francais (LIA CRIBs), Rennes, France*

^e*Department of Ultrasound, The Third People's Hospital of Shenzhen, Shenzhen, China*

^f*School of Biomedical Engineering, Sun Yat-Sen University, Guangzhou, China*

^g*Department of Medical Imaging, Western University, London, Canada*

^h*Digital Imaging Group of London, London, Canada*

Abstract

Accurate direct estimation of the left ventricle (LV) multitype indices from two-dimensional (2D) echocardiograms of paired apical views, i.e., paired apical four-chamber (A4C) and two-chamber (A2C), is of great significance to clinically evaluate cardiac function. It enables a comprehensive assessment from multiple dimensions and views. Yet it is extremely challenging and has never been attempted, due to significantly varied LV shape and appearance across subjects and along cardiac cycle, the complexity brought by the paired different views, unexploited inter-frame indices relatedness hampering working effect, and low image quality preventing segmentation. We propose a paired-views LV network (PV-LVNet) to automatically and directly estimate LV multitype indices from paired echo apical views. Based on a newly designed Res-circle Net, the PV-LVNet robustly locates LV and

*Corresponding author.

Email addresses: chenyang.list@seu.edu.cn (Yang Chen), sli287@uwo.ca (Shuo Li)

automatically crops LV region of interest from A4C and A2C sequence with location module and image resampling, then accurately and consistently estimates 7 different indices of multiple dimensions (1D, 2D & 3D) and views (A2C, A4C, and union of A2C+A4C) with indices module.

The experiments show that our method achieves high performance with accuracy up to $2.85mm$ mean absolute error and internal consistency up to 0.974 Cronbach's α for the cardiac indices estimation. All of these indicate that our method enables an efficient, accurate and reliable cardiac function diagnosis in clinical.

Keywords: multitype cardiac indices, direct estimation, 2D echo, paired apical views, Res-circle Net

1. Introduction

Accurate estimation for left ventricle (LV) indices (i.e., dimension, area & volume) in two-dimensional (2D) echocardiograms (echo) of paired apical views (i.e., paired apical four-chamber and two-chamber views) is of great clinical significance to cardiac function evaluation (Schiller et al., 1989; Lang et al., 2006, 2015). 2D echo is the most frequently used noninvasive modality for the diagnosis of cardiac disease because of its unique ability to provide real-time images of the beating heart, combined with its availability and portability (Lang et al., 2015; Abdi et al., 2017; Gao et al., 2017, 2018). The multitype indices of LV from 2D echo paired apical views, covering long-axis dimension (LAD), short-axis dimension (SAD), area and volume, which are measured from cavity as Fig.1, are most widely used to assess LV chamber size and contractile function (Schiller et al., 1989; Pascual et al., 2003; Lang et al., 2015). It promotes comprehensive metrics from 1D (i.e., LAD, SAD), 2D (i.e., area) and 3D (i.e., volume). Such paired orthogonal apical four-chamber (A4C) and two-chamber (A2C) views enable a better stereoscopic reproducibility of cardiac LV motion compared to the separate plane observation from single view, for further comprehensive quantitative functional analysis (Schiller et al., 1989; Ciampi and Villari, 2007).

The existing (semi-)automated cardiac indices estimation methods never refers to multitype indices in 2D echo sequences of paired apical views. These methods are mainly classified into two groups: segmentation and direct regression. However, the segmentation methods just enable limited simple index types (i.e. area) without extra interaction, and the existing direct

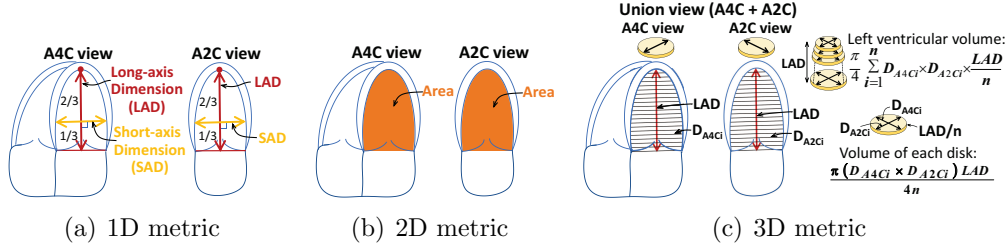


Figure 1: The multitype indices from the paired apical views (A2C & A4C) are critically important for clinical diagnosis, yet extremely laborious measurement. They cover the 1D and 2D metrics of each single view, and the 3D metric of union view, for a comprehensive assessment. (a) LAD: from the apex to the middle mitral valve plane. SAD: perpendicular to the long axis, at one-third of the LAD from the mitral valve plane. (b) Area: the whole LV cavity. (c) LV volume: jointly from A4C and A2C by using the biplane method of discs (modified Simpson’s rule).

25 methods almost all focus on a single view of cardiac magnetic resonance
 26 (CMR) causing limited observation and evaluation. Strong clinical evidence
 27 shows that the indices from echo that cover multiple dimensions and views
 28 enable a comprehensive cardiac diagnosis, yet their automated estimation is
 29 still thwarted by inherently existing challenges such as 1) LV shape and
 30 appearance in apical view significantly vary among subjects, and along
 31 the cardiac cycle. 2) Although the paired views provide complementary
 32 information, the different image structures are introduced with increased
 33 complexity. 3) Ambiguous relatedness inter frames hampers learning
 34 procedure of sequential indices from better convergence and generalization.
 35 4) Low image quality of echo, like fuzzy border, edge dropout, acoustic
 36 shadows, etc., raises great challenges for automated methods, especially
 37 segmentation method.

38 1.1. Related Works

39 **Segmentation methods** aim to achieve automated LV segmentation for
 40 improving the diagnosis efficiency, however it is still an open and challenging
 41 task, due to the inherent characteristics of the 2D echo, such as low signal-to-
 42 noise ratio, edge dropout, shadows, indirect relation between pixel intensity
 43 and the physical property of the tissue, and anisotropy of ultrasonic image
 44 formation (Carneiro et al., 2012). Active contours (Debreuve et al., 2001;
 45 Malladi et al., 1995; Paragios, 2003) and deformable templates (Jacob et al.,
 46 2002; Nascimento et al., 2008) achieve good segmentation results relying on

47 the LV shape and appearance of the prior knowledge (Georgescu et al., 2005).
48 By considering use of inaccurate prior knowledge and low-level handcrafted
49 features may bound working robustness, the supervised deep learning method
50 (Mo et al., 2018; Chen et al., 2016; Carneiro et al., 2012; Oktay et al., 2018)
51 tries to learn information from data. The deep Poincar Map (Mo et al., 2018)
52 coupled deep learning with the dynamic-based labeling scheme to reduce the
53 requirement on the huge data; iMD-FCN (Chen et al., 2016) used the transfer
54 learning from cross domains to enhance the feature representation; Carneiro
55 et al. (2012) combined the deep belief networks, the decoupling rigid and
56 nonrigid classifiers and the derivative-based search to increase the robustness
57 for imaging conditions and LV shape variations; ACNNs (Oktay et al., 2018)
58 encouraged the models to follow the global anatomical properties of the
59 underlying anatomy via the non-linear representations of the shape learnt
60 from the stacked convolutional autoencoder. All of these show great potential
61 with the development of deep learning. Nevertheless, most of the working
62 LV segmentation methods in the practical clinical diagnosis are still semi-
63 automatic, which need time-consuming user interaction to handle a great
64 number of medical images (Luo et al., 2018).

65 **Direct regression methods** without intermediate segmentation has
66 undergone a great development and recognition (Ravi et al., 2017; Peng
67 et al., 2016; Wu et al., 2017; Lathuilière et al., 2017; Pereira et al., 2018;
68 Zhen et al., 2014a, 2015b, 2017) for better and more efficient cardiac indices
69 estimation, but never performed on paired 2D echo apical views. By directly
70 analyzing LV biological structure, these methods provide effective tools to
71 automate the analysis of one single view from CMR, especially the short-
72 axis view, and enable accurate and efficient diagnosis in clinical practice
73 (Zhen et al., 2016). With two-phase operation, LV volume (as integration
74 of cavity areas in short-axis view slices) is estimated on the handcrafted
75 cardiac image representation, including Bhattacharyya coefficient between
76 image distributions (Afshin et al., 2012, 2014), appearance features (Wang
77 et al., 2014), multiple low level image features (Zhen et al., 2014b), as
78 well as unsupervised features from multiscale convolutional deep belief
79 network (Zhen et al., 2016) and supervised descriptor learning (Zhen et al.,
80 2015a). Instead of separate representation and regression, joint learning (Xue
81 et al., 2017a,c) captures task-relevant cardiac information for the indices
82 estimation. For a comprehensive assessment of cardiac function, Xue et al.
83 (2017b, 2018) achieve multitype indices estimation on short-axis view cardiac
84 CMR. However, all of these direct methods still have the limitation on

85 2D echo paired apical views, due to: 1) multitype indices estimation from
 86 different views is ignored and lacked, 2) some cardiac indices in 2D echo,
 87 like volume, are often obtained jointly from paired views, and 3) LV shape
 88 in apical view is irregular and make it difficult to establish a standard
 89 preprocessing method for getting LV cropping (short-axis view CMR just
 90 need to manually find several relatively fixed landmarks).

91 1.2. Contributions

92 In this paper, we propose a paired-views LV network (PV-LVNet) to
 93 automatically achieve a high-quality estimation of LV multitype indices from
 94 2D echo sequences of paired apical views. As shown in Fig.2, the network is
 95 built based on our newly designed Res-circle Net, and implemented with three
 96 interdependent functional parts: LV location module, image resampling and
 97 LV indices module. The Res-circle Net for sequential analysis embedded with
 98 subject’s holistic characteristics and frame’s temporal changes is used in both
 99 LV location and indices modules. And functionally, the LV location module
 100 with the anisotropic Euclidean distance loss shape-accordingly detects the
 101 LV center in echo apical views. The image resampling further crops the LV
 102 region of interest (LV-ROI) capable of efficiently reducing the interference of
 103 various structure from the different views. Accepting the LV-ROI, the LV
 104 indices module with the inter-frame gradient regularization and the views
 105 union effectively makes the comprehensive, accurate and internally consistent
 106 indices estimation.

107 The main contributions of our work include:

- 108 • For the first time, the proposed PV-LVNet enables an automatically
 109 and reliably comprehensive cardiac function clinical assessment from
 110 various dimensions and views by directly and accurately estimating LV
 111 multi-type indices on 2D echos of paired apical views.
- 112 • The newly designed Res-circle Net enables accurately and consistently
 113 estimating continuous changing centric positions and indices of LVs in
 114 echo sequence of each subject, by comprehensively combining both the
 115 subject-level base of cardiac cycle and the interrelated dynamic residual
 116 of each frame. Moreover, its residual transferring effectively reduces the
 117 gradient vanishing problem in recurrent net.
- 118 • The novel location loss in the form of anisotropic Euclidean distance
 119 (AED) guarantees robust and efficient location and cropping by
 120 matching the approximate bullet shape of LV in apical view echo.

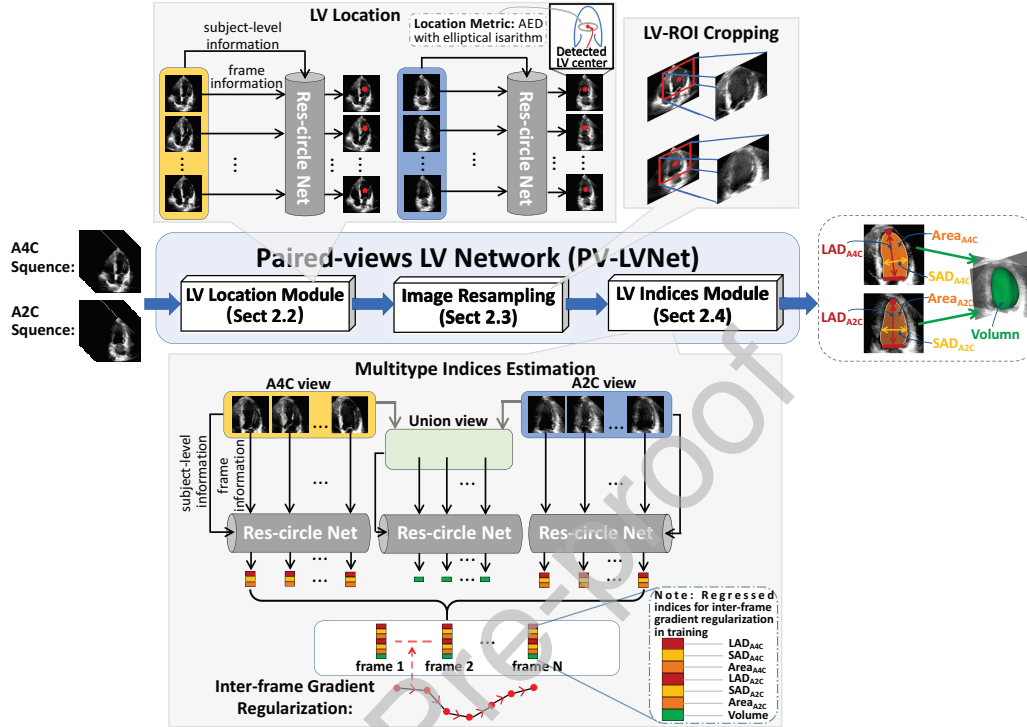


Figure 2: The PV-LVNet simultaneously estimates multitype indices of various single (A4C, A2C) and union views (A4C+A2C) from paired apical 2D echo sequences, to provide a comprehensive cardiac function assessment. Based on the Res-circle Net (Sect. 2.1), it has three interdependent parts: LV location module (Sect. 2.2) for LV location, image resampling (Sect. 2.3) for LV-ROI cropping and LV indices module (Sect. 2.4) for multitype indices estimation.

- 121 • The gradient of LV indices between adjacent frames in a cardiac cycle
 122 creatively and effectively enhances sequential indices fitting, by fully
 123 exploring inter-frame relatedness to introduce frame-by-frame evolution
 124 characteristic to regularize indices estimation.

125 2. Methodology

126 As shown in Fig.2, based on the **Res-circle Net (Sect. 2.1)** to analyze
 127 echo sequences, the PV-LVNet entirely works via three interdependent parts:
 128 **LV location module (Sect. 2.2)**, **Image Resampling (Sect. 2.3)** and **LV**
 129 **indices module (Sect. 2.4)** for location, cropping and indices estimation.

130 To enable the comprehensive and efficient echo sequence analysis, the novel
 131 Res-circle Net combines subject-level base for avoiding coarse sequential
 132 estimation from zero level and temporal dynamic residual for developing
 133 the refinement on each frame. To provide the robust LV location among
 134 views for accurate indices estimation, LV location module creatively adopts
 135 the loss in form of AED considering the LV shape in apical view echo.
 136 To automatically crop LV-ROI with the interference of various structure in
 137 paired views reduced, and build unblocked joint learning of location and
 138 indices regression, image resampling, as a differentiable transformation, is
 139 embedded. To achieve the various dimensional indices regression from single
 140 and union views, LV indices module performs not only indices-aware feature
 141 abstraction but also views union for 3D index. Moreover, to fulfill the inter-
 142 frame relatedness potential of indices for enhancing sequential data fitting,
 143 the inter-frames gradient in the time polyline of the cardiac index is used to
 144 deeply explore sequence evolution characteristics.

145 *2.1. Res-circle Net for Analyzing Echo Sequence*

146 The Res-circle Net combines both subject-level base and frame-level
 147 residuals for a comprehensive analysis on echo sequence. **Subject-level**
 148 **base** reflects the holistic characteristics among the different frames of
 149 the same subject. It gives a whole and inherent expression on the echo
 150 sequence and distinguishes different subjects. It is further extracted from
 151 the representations of all frames. **Frame-level residual** reflects interrelated
 152 temporal dynamic changes in the cardiac cycle. It enables a further
 153 refinement on each frame. It is extracted by using the inter-frame relationship
 154 among the whole cardiac cycle. The Res-circle Net captures interrelated
 155 temporal residual of each frame, then adds the residual with subject-level
 156 base together. It embeds subject and temporal information to guarantee
 157 a stable and dynamic estimation for location and indices in continuous
 158 moving and deforming LV. The net is implemented in the circle recurrent
 159 of a novel residual learning and transferring convolutional unit named as
 160 residual recurrent unit (RRU).

161 As shown in Fig.3, the Res-circle Net accepts current frame representation
 162 and links it to the integrated former residuals of the frames in the cycle,
 163 then adaptively updates the current frame-level residual and combine the
 164 residual with the subject-level base for a refined outputting. The Res-circle
 165 Net is achieved in the circle recurrent structure (Graves, 2012; Xue et al.,
 166 2017c) of RRU, which gives the memory characteristics of the cycle temporal

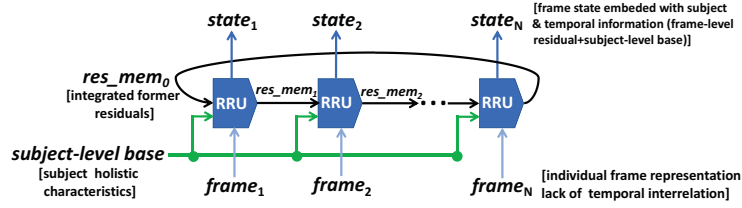


Figure 3: The Res-circle Net embeds both subject and interrelated temporal information together for comprehensive and reliable analysis on the echo sequence. It adaptively updates current dynamic change as residual by linking the current frame representation with the former memory in cycle, then adds such residual with the subject-level base together as the comprehensive state of the frame.

167 changes. Similar works to analyze data sequence can be seen in using LSTM
 168 of recurrent neural networks (RNN) as: Xu et al. (2018) adopt fully connected
 169 LSTM (FC-LSTM) for the dependence crossing over a long time interval; Xue
 170 et al. (2017c) further deployed circle FC-LSTM for shortening the distance
 171 between the first and last frames; and convolutional LSTM (Xingjian et al.,
 172 2015) was developed for the spatial structure in the sequence. Specially, our
 173 Res-circle Net of circle recurrent convolutional residual net is designed for
 174 temporally-spatially modeling the residuals among frames and the entirety
 175 of sequence, to the echo of dynamic and consecutive data.

176 The RRU has both functions of current frame state prediction and
 177 residuals memory integration, as shown in Fig.4. In the output path, the
 178 RRU provides the current state ($state_i$) for the followed regression, by adding
 179 current frame-level residual (res_i) on the subject-level base ($base$). In the
 180 hidden path, it transfers residual information (res_i) together with the formers
 181 ($res_{mem_{i-1}}$) to integrate residuals memory (res_{mem_i}) for the next frame.
 182 Instead of the frame-wise coarse estimation from the zero level, the net
 183 provides such a more refined way as the subject-level base reflects the stable
 184 base level of sequence and residual focuses on interrelated dynamic change of

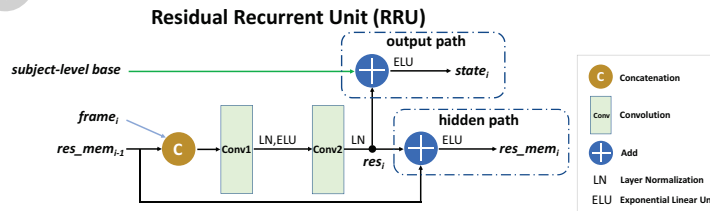


Figure 4: Residual recurrent unit (RRU) has both functions of current frame state prediction and residual transfer. In output path, the current frame-level residual is added to the subject-level base for followed regression. In hidden path, the residual information is transferred together with the formers for the next frame.

185 each frame. Benefited from the residual connection with subject-level base
 186 and former residuals, the net has powerful sequence analysis and temporal
 187 modeling, and meanwhile effectively reduces the gradient vanishing problem
 188 with the shortcut connection (Szegedy et al., 2017; He et al., 2016a,b).

189 The RRU takes both spatial structure and temporal information into
 190 account. It uses convolution process, instead of full connection in traditional
 191 RNN, to extract feature for keeping spatial correlation in the cardiac image.
 192 In recurrent way, it maps the current frame to the integrated residual memory
 193 to get its current frame-level residual. The inherent potential spatiotemporal
 194 characteristic in echo sequence is effectively mined and transmitted. Given
 195 the inputting individual frame representation $frame_i$ at each time step i ,
 196 the memory res_mem_{i-1} from the previous frames, and the subject-level
 197 base $base$, RRU gets the current frame-level residual res_i for the updated
 198 memory res_mem_i and outputting state representation $state_i$, as:

$$\begin{aligned} res_i &= LN(ELU(LN((frame_i \oplus res_mem_{i-1}) * W_1 + b_1)) * W_2 + b_2) \\ res_mem_i &= ELU(res_i + res_mem_{i-1}) \\ state_i &= ELU(base + res_i) \end{aligned} \quad (1)$$

199 where W_1 and W_2 are convolutional kernels in Conv1 and Conv2, b_1 and b_2
 200 represents biases. \oplus means concatenation, $*$ is convolution operation, and
 201 LN , ELU denote the element-wise transformations of layer normalization
 202 (Ba et al., 2016) and exponential linear unit (Clevert et al., 2015).

203 2.2. LV Location Module for Detecting Left Ventricle Center

204 LV location module aims to detect continuously moving LV center in both
 205 A4C and A2C sequences, as in Fig.5. It has four steps: 1) **CNN-loc** firstly
 206 extracts cardiac subject-level base and individual frame representations of
 207 the cardiac sequence and feeds them to the res-circle net; 2) **Res-circle Net**
 208 then models sequential LV moving in cardiac cycle for the final location,
 209 with subject’s holistic position and frame’s temporal changes embedded;
 210 3) **Fully connected (FC) layer** further performs LV center coordinate
 211 regression with the output of Res-circle Net fed; And 4) **AED metric** is
 212 used to measure the regressed center with anisotropic scaling by considering
 213 approximate bullet shape of LV in echo apical views for robust location.

214 Advantageously, LV Location Module is benefited from the special design
 215 of **CNN-loc** and **AED location metric**, besides Res-circle Net that has
 216 been proposed in Sect. 2.1.

217 **CNN-loc.** To get expressive and task-aware representation of individual
 218 frame and entire subject on the paired echo sequences, CNN-loc consists

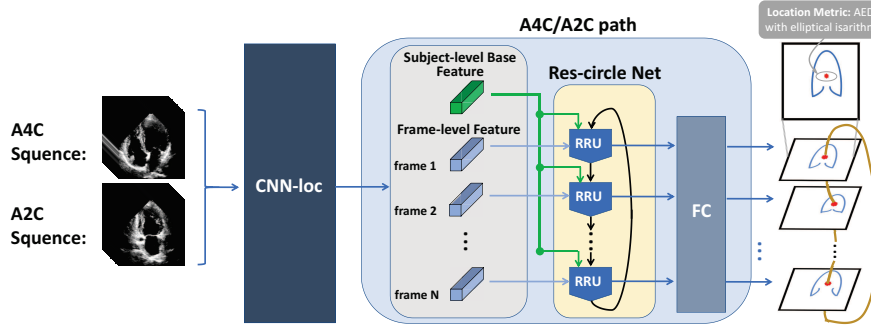


Figure 5: To achieve locating continuously changing center of LV in both A4C and A2C sequences, LV location module works via: 1) CNN-loc extracts subject-level base and frame representations for both paired views. 2) Res-circle Net captures residual information of each frame by leveraging inter-frame relationship for modeling dynamic changes, and further combine subject-level base to provide the frame state for location. 3) FC layer linearly regresses LV center coordinate. 4) The metric of anisotropic Euclidean distance (AED) ensures the robust location.

219 of several shared layers for general expression and two shallow paths that
 220 further refine on A4C and A2C respectively considering big view difference
 221 and enhancing robustness, as shown in Fig.6 (a). The individual cardiac
 222 distribution in each frame is extracted by the hierarchical convolutions, and
 223 the global sequence base of the subject is then captured by concatenating
 224 all these individual representations together with a further convolution
 225 operation followed so that holistically characterizes all frames. The backbone
 226 structure of CNN-loc is the stack of the successive convolutional blocks (He
 227 et al., 2016a) in Fig.6 (b), which chooses identity map for the layer input
 228 and output of the same size, or convolution of kernel size 1×1 to match
 229 dimensions. Such block promotes information propagation both forward and

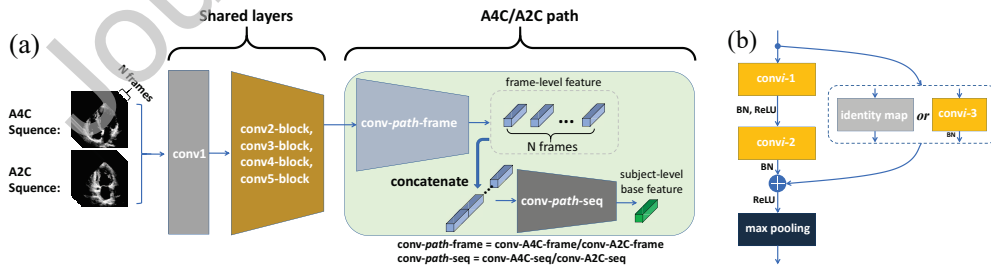


Figure 6: CNN-loc gets subject-level base and frame representation of paired echo sequences. (a) CNN-loc is composed of several shared layers and two shallow paths refined on A4C and A2C. (b) The stacked block in CNN-loc. The use of short-cut connection accelerates the net convergence and improve learning performance.

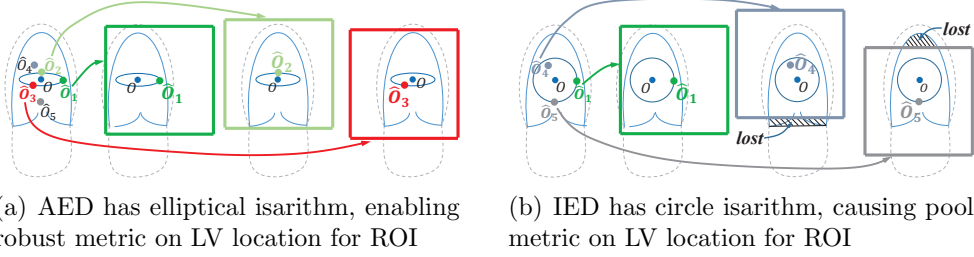


Figure 7: The anisotropic Euclidean distance (AED) provides an elliptical isarithm to match the approximate bullet shape of LV in apical view echo and enable a more reasonable and robust LV location metric than the isotropic Euclidean distance (IED). (a) Considering LV shape, AED gives different scaling on the horizontal and vertical direction to construct elliptical isarithm for efficient LV location in apical view echo. (b) IED causes pool metric on LV location due to its circle isarithm.

backward and hence accelerate the net convergence and improve learning performance (Szegedy et al., 2017; Yu et al., 2017). The configurations of the stacked convolutions in CNN-loc are: $7 \times 7 \times 64$ with stride 2 for conv1, $channel = 64, 128, 128, 256, 256$ for convolutional blocks (conv{2,3,4,5}-block and conv-path-fram), and $3 \times 3 \times 256$ with stride 1 for conv-path-seq.

AED location metric. To achieve a structure matching location measurement, anisotropic Euclidean distance (AED) is deployed on the regressed center with the different metric scaling on horizontal and vertical directions, as shown in Fig.7 (a). Differently and traditionally, the location metric generally uses strict isotropic Euclidean distance (IED) in Eq. (2), where the regressed result $\hat{O} = (\hat{o}_x, \hat{o}_y)$ and the ground truth $O = (o_x, o_y)$.

$$distance_{IED} = \|O - \hat{O}\| \quad (2)$$

However, the shape of the LV is approximate to the bullet, so that the regressed points with same IED values still cause different influences to the ROI, and smaller IED does not mean a more accurate location. For example, \hat{O}_1 and \hat{O}_5 in Fig.7 (b) fall on the same circle isarithm of the IED to the LV center O , and \hat{O}_4 even has smaller IED than \hat{O}_1 . But only the \hat{O}_1 centered square contains the entire LV cavity, while \hat{O}_4 and \hat{O}_5 lead to the weak ROIs.

In order to overcome the shortcoming in IED, AED using anisotropic scaling is a more reasonable metric that conforms to the LV shape. Comparing Figs.7 (a) with (b), \hat{O}_4 and \hat{O}_5 that have the same IED value as \hat{O}_1 or smaller than \hat{O}_1 are outside the elliptical isarithm of AED, which means getting higher AED metric. It aligns with their poor ROI quality in Fig.7 (b). Besides, the ROIs centered by the points \hat{O}_2 and \hat{O}_3 that fall on the ellipse in Fig.7 (a) have the same ROI situation as \hat{O}_1 , that the entire

254 LV cavity is contained and close to the square border, and gains the same
 255 metric. Therefore, the AED introduces a more robust and effective location
 256 metric for LV. The AED calculation is given in Eq. (3).

$$distance_{AED} = \sqrt{\beta \cdot (\hat{o}_x - o_x)^2 + (1 - \beta) \cdot (\hat{o}_y - o_y)^2} \quad (3)$$

257 2.3. Image Resampling for Cropping LV-ROI

258 Image resampling is implemented via spatial transform and bilinear
 259 interpolation to automatically crop LV-ROI according to the location from
 260 Sect. 2.2. Image resampling puts attention on determining the region most
 261 related to the LV. It aims to reduce the disturbance from the other pathology
 262 caused by various structure and extra chambers in different views, with the
 263 LV-ROI being cropped. Also, the LV-ROI sequence maintains the relative
 264 shapes of LVs among different frames to not destroy the inherent subject
 265 characteristics and frame-by-frame LV dynamic changes along the cardiac
 266 cycle for developing the sequential LV indices estimation of each subject. In
 267 a similar work, Dai et al. (2016) used ROI warping layer to crop feature map
 268 regions for refining further semantic segmentation. Additionally, Jaderberg
 269 et al. (2015) and Vigneault et al. (2018) used STN to spatially transform
 270 intermediate feature maps or inputting image for improving performance in
 271 classification and medical segmentation, respectively.

272 In our work, the image resampling transforms the images into the pattern
 273 that are centred on the predicted LV centre, and crops them to the predefined
 274 dimensions images. Given the predicted LV centre $\hat{O} = (\hat{o}_x, \hat{o}_y)$ and the
 275 source echo image I , the target LV-ROI image $I^{ROI}(\hat{O})$ is obtained by the
 276 image resampling as formulated as the differentiable linear transformation:

$$I^{ROI}(\hat{O}) = B(T(\hat{O})) \cdot I. \quad (4)$$

277 In Eq. (4), $T(\cdot)$ is the spatial transform that firstly translates the echo
 278 image I horizontally and vertically to be centred on \hat{O} and then scales
 279 the translated image to crop a $153.6\text{ pixel} \times 153.6\text{ pixel}$ image (physical
 280 dimensions $79.49 \sim 115.80\text{ mm} \times 79.49 \sim 115.80\text{ mm}$ with pixel space
 281 $0.5175\text{ mm/pixel} \sim 0.7539\text{ mm/pixel}$) centred on the predicted LV centre.
 282 $B(\cdot)$ means bilinear interpolation further calculates the pixel value and
 283 produces the LV-ROI in a sufficiently fine resolution which is set as same
 284 as the original echo image, for the following indices estimation.

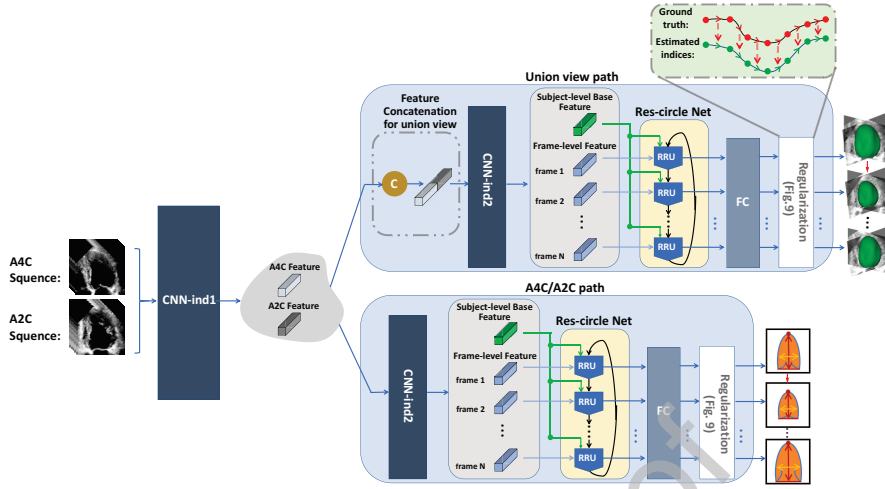


Figure 8: To estimate multitype indices from single/union views, LV indices module works via: 1) CNN-ind1+Feature Concatenation+CNN-ind2 gets feature representation on both entire subject and individual frame for all single and union views. 2) Res-circle Net models frame-by-frame dynamic residuals in the cardiac cycle by inter-frame relationship, then add them with the subject-level base of the holistic shape, for embedding subject and temporal information. 3) FC layer regresses indices with the outputs of the Res-circle Net. 4) Inter-frames gradient regularizes indices changes among frames to enhance sequential indices estimation.

285 2.4. LV Indices Module for Estimating Multitype Indices

286 LV indices module is designed to estimate multitype sequential cardiac
 287 indices in union and single views from continuously deformed LVs, as shown
 288 in Fig. 8. It consists of four components: 1) **CNN-ind1 + Feature**
 289 **Concatenation + CNN-ind2** makes frame and subject feature extraction,
 290 as well as union view representation. 2) **Res-circle Net** combines subject
 291 holistic shape and temporal deformation. 3) **FC layer** further regresses on
 292 the feature representation from Res-circle Net to estimate all indices. And 4)
 293 **Inter-frames Gradient** is meanwhile introduced to regularize the indices
 294 evolution among frames.

295 The superiority of LV indices module benefits from the special in
 296 **CNN-ind1 + Feature Concatenation + CNN-ind2** and **Inter-frames**
 297 **Gradient Regularization**, besides Res-circle Net demonstrate in Sect. 2.1.

298 **CNN-ind1 + Feature Concatenation + CNN-ind2**. In order to
 299 get both the frame and the subject features for all union and single views,
 300 it is further split and developed from CNN-loc that CNN-ind1 conducts the
 301 preliminary view-specialized representation on paired fed A4C and A2C ROI
 302 sequence, Feature Concatenation integrates the union view information via

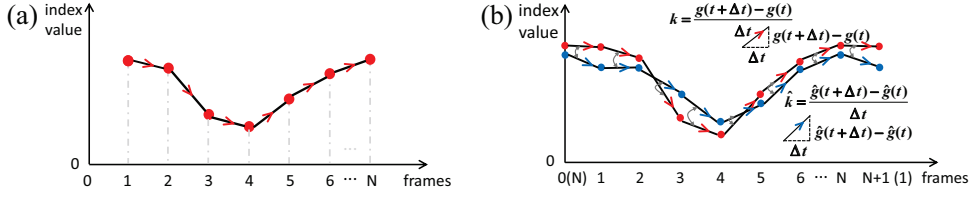


Figure 9: Inter-frames gradient regularization promotes sequential indices regression. (a) Frame-by-frame evolution of index is reflected by the polyline of index value vs. frame. (b) Inter-frames gradient regularizes frame-by-frame evolution of estimated results to strengthen sequential indices fitting. It reveals index changes among frames, and thus characterizes index evolution. Evolution is an important metric in measuring the similarity between two sequential data.

303 unifying the A4C and the A2C representations along the feature channel,
 304 and CNN-ind2 of the individual and the holistical features extraction is
 305 further performed on all the A4C, A2C and union view. In the procedure,
 306 the union view aims to construct the 3D spatial information from the two
 307 orthogonal views for the volume of 3D indices estimation and meanwhile
 308 further strengthening the contact among all views.

309 **Inter-frames Gradient Regularization.** For the accurate sequential
 310 indices estimation, the gradient inter frames is used with considering the
 311 evolution characteristics in the cardiac cycle. The frame-by-frame evolution
 312 of index in the cardiac cycle is shown in Fig. 9(a) with the polyline of index
 313 value vs. frame, it reflects the trend over time. And the gradient can be
 314 explored to depict these evolution characteristics of time polyline in 9(a),
 315 so that enhance the sequential indices fitting elegantly with the interrelated
 316 fluctuation regularized on the sequence of the preliminary regressed index. As
 317 shown in 9(b), it measures the slope of the secant passing through adjacent
 318 discrete points. Given the regressed result \hat{y}^f , and normalized the frame
 319 interval Δt as ± 1 for both adjacent frames, the inter-frames gradient \hat{k}^f at
 320 each frame step is defined as:

$$\hat{k}^f = (\hat{k}^{f-}, \hat{k}^{f+}), \text{ and } \begin{cases} \hat{k}^{f-} = \hat{y}^f - \hat{y}^{f-1} \\ \hat{k}^{f+} = -(\hat{y}^f - \hat{y}^{f+1}) \end{cases} \quad (5)$$

321 where \hat{k}^{f-} and \hat{k}^{f+} mean left and right gradient of frame f , respectively. \hat{k}^f
 322 thus effectively characterizes index evolution of frame f between adjacent
 323 frames $f - 1$ and $f + 1$.

324 Therefore, the inter-frames gradient of each index among the cardiac cycle
 325 is introduced to fit the trend of polylines of regressed results and ground
 326 truth, as shown in Fig. 9(b), to enhance sequential LV indices estimation.
 327 Euclidean distance is used to calculate the gap of the change rate of each

328 frame between regressed results and ground truth. The fitness of sequential
 329 indices evolution is measured as Eq. (6). In addition to the fitting of
 330 each index value, such evolution of the index further gives full play to the
 331 constraint between adjacent frames, and can be used as a regularization item
 332 to strengthen sequential objects estimation.

$$Reg_{grad} = \sum_{f=1}^N \sum_t \left\| k_t^f - \hat{k}_t^f \right\|_2 \quad (6)$$

333 where $f \in \{1, 2, \dots, N\}$ for all frames in cardiac cycle, $t \in \{LAD_{A4C}, SAD_{A4C},$
 334 $Area_{A4C}, LAD_{A2C}, SAD_{A2C}, Area_{A2C}, Volume\}$ for all index types.

335 3. Joint Loss Function for Different Tasks

336 The loss function in our work is designed for optimizing the two trainable
 337 modules (LV location module and indices module, while image resampling,
 338 as a powerful linear transformation, needs no training) of different tasks in
 339 the integrated PV-LVNet, so that the task-inter relevance and dependence
 340 enable the modules to mutually promote refinement of each other. The joint
 341 loss \mathcal{L}_{joint} is constructed as:

$$\mathcal{L}_{joint} = \lambda_1 \mathcal{L}_{loc} + \lambda_2 \mathcal{L}_{ind} + \lambda_3 R(\theta) \quad (7)$$

342 where \mathcal{L}_{loc} and \mathcal{L}_{ind} are the loss functions of location and indices estimation,
 343 $R(\theta) = \|\theta\|_2^2$, known as Tikhonov regularization for improving the training
 344 generality, is used as the regularization item of the network parameter vector
 345 θ with l_2 -norm. λ_1 , λ_2 and λ_3 are set as 1000.0, 1.0 and 0.1.

346 The location loss function \mathcal{L}_{loc} aims to guarantee a robust location of LV
 347 for LV-ROI cropping. It is constructed with AED for taking account of the
 348 approximate bullet shape of LV. The definition of \mathcal{L}_{loc} is given by:

$$\mathcal{L}_{loc} = \frac{1}{N} \sum_{f=1}^N distance_{AED}^f \quad (8)$$

349 where $distance_{AED}^f$ denotes $distance_{AED}$ (defined in Eq. (3)) for the
 350 predicted centre in each frame f .

351 The indices loss function \mathcal{L}_{ind} aims to boost high-quality indices
 352 regression. It utilizes not only the MAE of indices value estimation error
 353 in each frame but also the trend between indices of adjacent frames for both
 354 accuracy and inter consistency of the sequential indices estimation, as:

$$\mathcal{L}_{ind} = \frac{1}{N} \sum_t \sum_{f=1}^N \left| \hat{y}_t^f - y_t^f \right| + Reg_{grad} \quad (9)$$

355 where the first item is the MAE loss of indices, Reg_{grad} (defined as Eq.(6))
 356 is the inter-frames gradient regularization item for indices evolution.

357 4. Experiment Configurations

358 **Dataset.** A dataset of 2D echos with the ground truth is used to evaluate
 359 our method, which includes 2000 echo images from 50 subjects collected from
 360 2 hospitals. Each subject provides both paired A4C and A2C views echos,
 361 with the temporal resolution of 20 frames per cardiac cycle and the resize of
 362 256×256 . All ground truth of location and indices are manually annotated
 363 by two experienced cardiac radiologists with double-checking. In training,
 364 location labels are normalized to $[-1, 1] \times [-1, 1]$ through subtracting half of
 365 the image dimension (128) and then being divided by the image dimension
 366 (256). The labels of 1D (i.e., LAD_{A4C} , SAD_{A4C} , LAD_{A2C} and SAD_{A2C}), 2D
 367 (i.e., $Area_{A4C}$ and $Area_{A2C}$) and 3D (i.e., $Volume$) metrics are normalized by
 368 LV-ROI dimension ($\frac{256}{p}$, where $\frac{1}{p} = 0.6$ is set according to prior investigation
 369 on our dataset), area ($(\frac{256}{p})^2$) and volume ($(\frac{256}{p})^3$), respectively.

370 **Data Augmentation.** To avoid the over-fitting and improve the
 371 generalization, we augment the dataset to 8000 images by three strategies as:
 372 1) randomly rotating between -15° and 15° ; 2) randomly zooming between
 373 0.9 and 1.1 times; and 3) the combination of random rotation + zoom.

374 **Configurations.** The net is implemented by Tensorflow, and performed
 375 on NVIDIA P100 GPU. Ten-fold cross validation is employed for performance
 376 evaluation and comparison.

377 **Evaluation Metrics.** We evaluate the performance of the PV-LVNet in
 378 terms of estimation accuracy and internal consistency for multitype indices
 379 of all frames in the cardiac cycle. The evaluation is performed with two
 380 metrics including: the mean absolute error (MAE) for measuring accuracy
 381 and Cronbach's α (Cronbach, 1951) for measuring internal consistency
 382 between the estimated results and the corresponding ground truth. Denote
 383 the estimated cardiac index and ground truth of the i th subject and
 384 the f th frame as $\hat{y}_{t,i}^f$ and $y_{t,i}^f$, where $t \in \{LAD_{A4C}, SAD_{A4C}, Area_{A4C},$
 385 $LAD_{A2C}, SAD_{A2C}, Area_{A2C}, Volume\}$ for index types. The MAE of each
 386 cardiac index is given by $MAE_t = \frac{1}{S \times N} \sum_{i=1}^S \sum_{f=1}^N |\hat{y}_{t,i}^f - y_{t,i}^f|$, where S and
 387 F are the number of subjects and frames, respectively. Cronbach's α of
 388 each cardiac index is calculated as $\alpha_t = 2 \cdot (1 - \frac{\sigma_{\hat{y}_t}^2 + \sigma_{y_t}^2}{\sigma_{\mathcal{X}_t}^2})$, where \mathcal{X}_t is the sum
 389 of estimated indices $\hat{\mathcal{Y}}_t = \{\hat{y}_{t,1}^1, \hat{y}_{t,1}^2, \hat{y}_{t,1}^3, \dots, \hat{y}_{t,S}^N\}$ and corresponding ground

390 truth $\mathcal{Y}_t = \{y_{t,1}^1, y_{t,1}^2, y_{t,1}^3, \dots, y_{t,S}^N\}$, i.e., $\mathcal{X}_t = \hat{\mathcal{Y}}_t + \mathcal{Y}_t$. Moreover, $\sigma_{\hat{\mathcal{Y}}_t}^2$, $\sigma_{\mathcal{Y}_t}^2$ and
 391 $\sigma_{\mathcal{X}_t}^2$ are the corresponding variances for $\hat{\mathcal{Y}}_t$, \mathcal{Y}_t and \mathcal{X}_t .

392 5. Results and Analysis

393 We conduct a set of experiments to evaluate the performance of our
 394 proposed PV-LVNet, including: 1) overall performance; 2) effectiveness of
 395 res-circle net; 3) effectiveness of anisotropic Euclidean distance location
 396 loss; 4) effectiveness of inter-frames gradient regularization; 5) performance
 397 comparison with relevant methods; 6) performance of activation function and
 398 Hyper parameter selection.

399 5.1. Overall Performance

400 As shown in the last column of Table 1, the proposed PV-LVNet achieves
 401 excellent estimation accuracy and internal consistency on all the 7 different
 402 indices, which are attributable to comprehensively analyzing sequential
 403 echos, robustly locating and cropping LV, deeply exploiting inter-frame
 404 indices relatedness. It gains extremely low MAE of $2.85mm$, $3.16mm$,
 405 $3.06mm$, $2.98mm$, $287mm^2$, $264mm^2$ and $10.7ml$ for LAD_{A2C} , SAD_{A2C} ,
 406 LAD_{A4C} , SAD_{A4C} , $Area_{A2C}$, $Area_{A4C}$ and $LV\ volume$, as well as high
 407 Cronbach’s α all exceeding 0.9, with the manually obtained ground truth.

408 Moreover, our proposed PV-LVNet also achieves high coincide indices
 409 estimation along the cardiac cycle, indicating powerfully modeling the LV
 410 activity. As shown in Fig. 10, it reaches extremely low normalized
 411 root-mean-square error of 1.26% (NRMSE, $NRMSE = \frac{1}{\bar{y}} \sum_{f=1}^N \frac{(\hat{y}^f - y^f)^2}{N}$)
 412 with the sequential ground truth, on average. Such rare few deviations
 413 strongly validate that the network effectively captures the activity pattern
 414 of sequential LVs.

415 Our method is also very efficient in running time. The training takes 16.36
 416 hours with one P100 GPU. The testing takes only 0.70 seconds per subject.
 417 Clearly, our method enables a real-time solution for clinical application.

418 5.2. Effectiveness of Res-circle Net

419 As shown in Table 2, the Res-circle Net decreases the MAE by 15.7% (e.g.,
 420 $15.7\% = \frac{1}{7} [\frac{3.46-2.85}{3.46} + \frac{3.64-3.16}{3.64} + \frac{3.37-3.06}{3.37} + \frac{3.24-2.98}{3.24} + \frac{336-287}{336} + \frac{321-264}{321} + \frac{15.1-10.7}{15.1}]$)
 421 and gains exceeding 0.9 Cronbach’s α on all indices, compared to the
 422 the situation of being replaced by CNN in the PV-LVNet for revealing
 423 its effectiveness. By combining subject-level holistic characteristics and

Table 1: The proposed method gains most advanced performance in the various dimensional metrics for LV of all views compared to the existing methods. It achieves higher accuracy and more excellent internal consistency, with lower MAE (18.9% ↓) and higher Cronbach’s α (> 0.9) for each LV index. MAE and α are shown in each cell.

	Multi-features+RF	SDL+AKRF	MCDBN+RF	Indices-Net	U-Net	PV-LVNet
One-dimensional Metric (<i>mm</i>)						
<i>LAD</i> _{A2C}	3.52±3.10 0.895	3.29±2.48 0.913	3.44±3.18 0.898	3.19±2.43 0.923	/	2.85±2.46 0.941
<i>SAD</i> _{A2C}	3.76±3.02 0.890	4.51±3.34 0.866	3.81±3.13 0.895	3.60±2.82 0.910	/	3.16±2.68 0.930
<i>LAD</i> _{A4C}	3.86±3.48 0.864	3.73±3.05 0.904	3.93±3.38 0.863	3.29±2.42 0.896	/	3.06±2.73 0.932
<i>SAD</i> _{A4C}	3.23±2.91 0.901	3.21±2.82 0.907	3.18±3.00 0.903	4.27±3.37 0.887	/	2.98±2.85 0.917
Two-dimensional Metric (<i>mm</i> ²)						
<i>Area</i> _{A2C}	331±259 0.870	321±274 0.884	320±264 0.885	361±431 0.876	393±338 0.887	287±284 0.907
<i>Area</i> _{A4C}	323±266 0.902	280±236 0.934	312±255 0.915	354±338 0.885	392±305 0.901	264±228 0.940
Three-dimensional Metric (<i>ml</i>)						
<i>Volume</i>	16.1±14.2 0.918	16.4±14.6 0.922	16.1±14.0 0.925	15.3±8.7 0.938	/	10.7±7.6 0.974

interrelated temporal changes existing in echo sequence, the Res-circle Net outperforms CNN which just performs independent processing for each frame, on accuracy and internal consistency. Adding subject-level base and interrelated dynamic residual of each frame together, the res-circle net enables and enhances refined sequential indices estimation by leveraging inter-frame temporal relationship and avoiding coarse estimation on each separate frame from zero level to improve accuracy. Moreover, introducing subject-level and temporal characteristics, the Res-circle Net guarantees excellent internal consistent estimation across subjects and among frames with the ground truth.

5.3. Effectiveness of AED location loss

As shown in Table 3, the AED location loss ensures developing accurate indices estimation. Compared with using IED in location, the AED location loss significantly decreases the MAEs by 21.3%, 11.0%, 13.8% and 30.5% on LAD, SAD, area and volume on average. These improvements are resulted from the fact that IED location loss effectively provides a robust and efficient location and cropping for indices estimation. It suits LV in apical view echo by adopting different scaled metrics on different directions to match

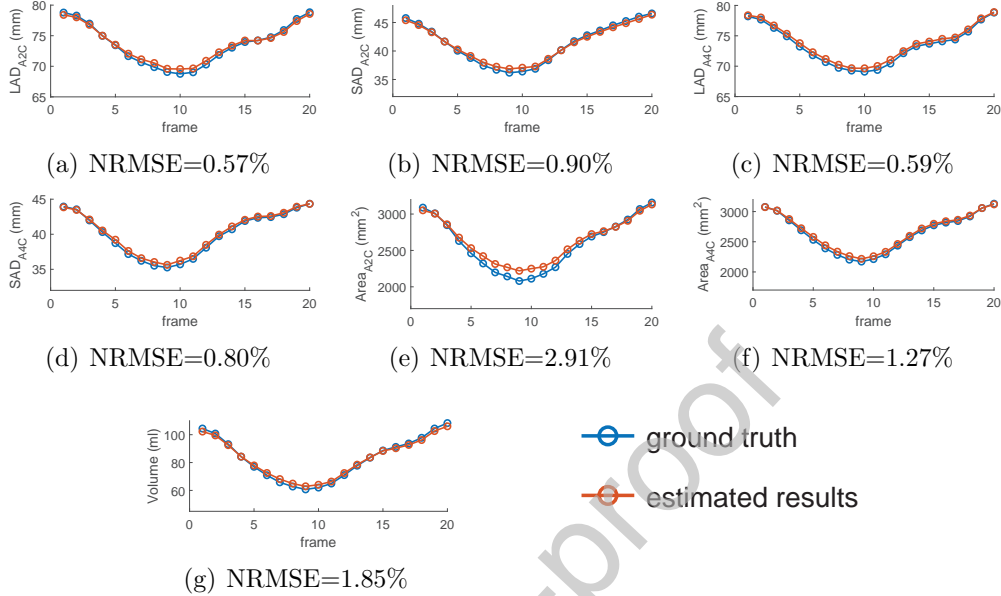


Figure 10: The proposed PV-LVNet effectively achieves high coincide indices estimation along the cardiac cycle to model the LV activity. The polygonal lines reflect the frame-wise value of each index for average subject. The normalized root mean square error (NRMSE) is used to measure the deviation between the polygonal lines of the estimated value and ground truth. As the results show, the network gains low NRMSE of 1.26% on average, with rarely few deviations.

442 the approximate bullet shape that is more strict on locations in the vertical
 443 direction than the horizontal direction, while the general IED loss can only
 444 provide a low-quality metric of no direction difference. Thus, LAD, area and
 445 volume which are extremely sensitive to vertical direction location get the
 446 highest improvements. Additionally, the SAD which is the most difficult to
 447 be estimated due to its non-independent measurement and a certain degree
 448 dependence on LAD still gets an obvious improvement of 11.0% with more
 449 accurate LAD.

450 5.4. Effectiveness of Inter-frames Gradient Regularization

451 As shown in Table 4, the inter-frames gradient regularization is capable of
 452 increasing the internal consistency of the estimated results with the ground
 453 truth. It gains higher Cronbach's α exceeding 0.9 on all indices and increased
 454 from 0.914 to 0.934 on average. By measuring the index change rate between
 455 adjacent frames, the inter-frames gradient is used to fit indices frame-by-
 456 frame evolution in sequence. So that the estimated sequential indices are

Table 2: The Res-circle Net contributes to high estimation accuracy and excellent internal consistency. It obtains lower MAE (15.7% ↓) and higher Cronbach’s α (> 0.9) than being replaced by CNN.

	CNN	Res-circle Net
One-dimensional Metric (mm)		
LAD_{A2C}	3.46 ± 2.87 0.915	2.85 ± 2.46 0.941
SAD_{A2C}	3.64 ± 2.86 0.913	3.16 ± 2.18 0.930
LAD_{A4C}	3.37 ± 2.66 0.893	3.06 ± 2.73 0.932
SAD_{A4C}	3.24 ± 2.65 0.888	2.98 ± 2.85 0.917
Two-dimensional Metric (mm^2)		
$Area_{A2C}$	336 ± 279 0.885	287 ± 284 0.907
$Area_{A4C}$	321 ± 289 0.908	264 ± 228 0.940
Three-dimensional Metric (ml)		
$Volume$	15.1 ± 11.8 0.935	10.7 ± 7.6 0.974

457 regularized to get consistent variation with the ground truth.

458 Besides, the inter-frames gradient regularization also enhances sequential
 459 data fitting to ensure stable and accurate estimation across the whole cardiac
 460 cycle, as shown in Fig. 11. It not only gains consistently lower estimation
 461 error, but also increases the stability by 18.7% on average. The inter-frames
 462 gradient regularization mines indices inter-frame relatedness to learn the
 463 fluctuation across the cardiac cycle. Such fluctuation explicitly explores the
 464 constraints among indices of different frames to promote stable and accurate
 465 estimation and reduce pulse estimation error for sequential indices.

466 5.5. Performance Comparison with Relevant Methods

467 Our PV-LVNet achieves the most advanced performance in the various
 468 dimensional metrics for the LV of all views compared to the existing methods:
 469 1) the two-phase direct estimation including Multi-features+RF (Zhen et al.,
 470 2014b), SDL+AKRF (Zhen et al., 2015a), MCDBN+RF (Zhen et al., 2016);
 471 2) the end-to-end direct estimation, i.e, Indices-Net (Xue et al., 2017a); 3) the
 472 indirect estimation with segmentation U-net (Ronneberger et al., 2015). As
 473 shown in Table 1, our method significantly decreases the MAE by 18.9% on
 474 average on all indices, compared to these methods. Besides, it simultaneously
 475 maintains excellent internal consistency with the manually obtained ground
 476 truth by high Cronbach’s α all exceeding 0.9.

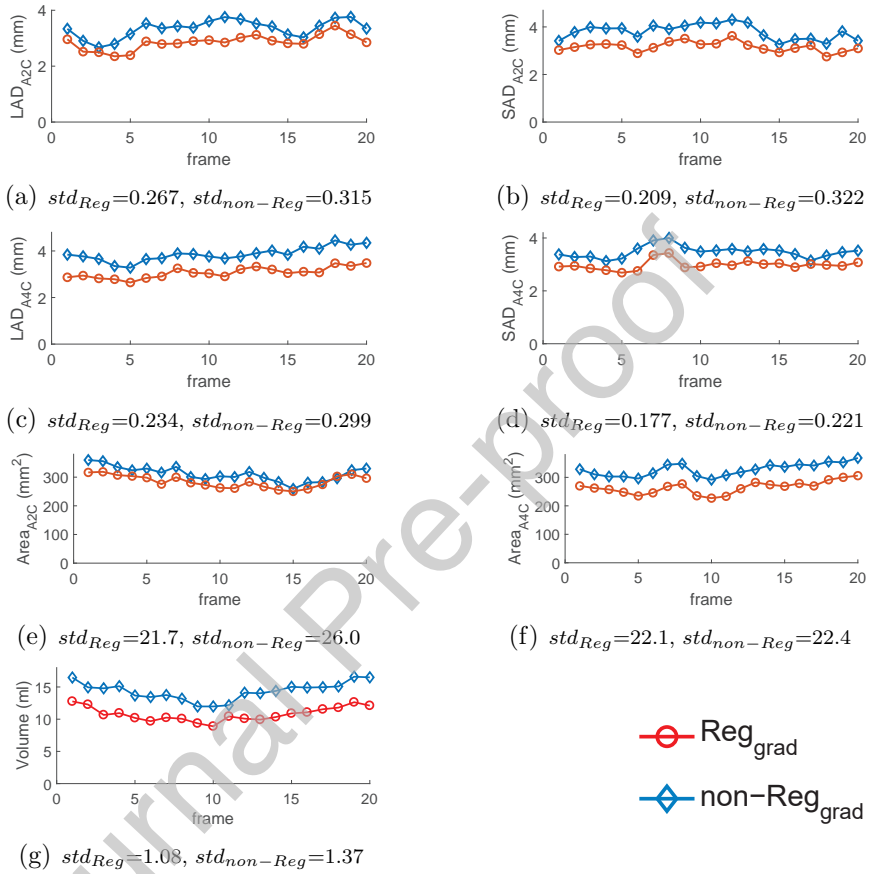


Figure 11: The inter-frames gradient well regularizes the network to enhance sequential data fitting. The polygonal lines record the frame-wise average MAE of each index. The standard deviation (std) is used to reflect the dispersion of MAE polygonal lines across a whole cardiac cycle. As the results show, using the inter-frames gradient regularization for the sequential indices decreased std by 18.7% compared to be removed, on average. It means stable and robust estimation on each frame. Also, the polygonal lines show consistently lower estimation error with inter-frames gradient regularization.

Table 3: The AED location loss ensures developing accurate estimation for LV indices. It brings higher estimation accuracy than the IED location loss, with lower MAE (17.3% ↓) on each type of cardiac indices.

	IED location loss	AED location loss
Long-axis Dimension (<i>mm</i>)		
<i>LAD_{A2C}</i>	3.89±2.89	2.85±2.46
<i>LAD_{A4C}</i>	3.62±2.38	3.06±2.73
<i>Average</i>	3.76±2.64	2.96±2.60
Short-axis Dimension (<i>mm</i>)		
<i>SAD_{A2C}</i>	3.48±2.84	3.16±2.68
<i>SAD_{A4C}</i>	3.41±2.84	2.98±2.85
<i>Average</i>	3.45±2.84	3.07±2.77
Area (<i>mm</i> ²)		
<i>Area_{A2C}</i>	322±255	287±284
<i>Area_{A4C}</i>	314±224	264±228
<i>Average</i>	318±240	274±259
Volume (<i>ml</i>)		
<i>Volume</i>	15.4±15.6	10.7±7.6

477 In detail, our method is superior to the relevant methods as:

478 1) The proposed PV-LVNet outperforms the two-phase direct method,
 479 with the average MAE decreased by 16.2%, 12.3% and 34.0% on 1D, 2D
 480 and 3D metrics, respectively. Different from these compared methods,
 481 the proposed method jointly learns the deep task-aware information and
 482 regresses target in an end-to-end way, instead of the split handcrafted feature
 483 extraction and regression. It is obviously validated on the volume estimation.
 484 The proposed method conducts a deeper learning on the concatenated feature
 485 jointly with volume estimation, and gets 34.0% improvement.

486 2) The proposed PV-LVNet outperforms the existing end-to-end direct
 487 method, with the average MAE decreased by 19.4% and all Cronbach's
 488 α increased to above 0.9. All of these are own to the fact that the
 489 proposed method effectively introduces the subject holistic characteristics
 490 and temporal changes for developing an accurate, stable and consistent
 491 estimation in a coarse-to-refine way, and deeply explores inter-frame indices
 492 relatedness for enhancing sequential indices estimation. However, the
 493 compared method just conducts separate estimation on each image.

494 3) The proposed PV-LVNet outperforms the segmentation method, with

Table 4: The inter-frames gradient regularization increases internal consistency with the ground truth. It gains higher Cronbach’s α (> 0.9) than being removed.

	non- <i>Reggrad</i>	<i>Reggrad</i>
One-dimensional Metric		
<i>LAD</i> _{A2C}	0.926	0.941
<i>SAD</i> _{A2C}	0.904	0.930
<i>LAD</i> _{A4C}	0.904	0.932
<i>SAD</i> _{A4C}	0.902	0.917
Two-dimensional Metric		
<i>Area</i> _{A2C}	0.897	0.907
<i>Area</i> _{A4C}	0.918	0.940
Volume		
<i>Volume</i>	0.945	0.974

495 estimating 5 more indices. It efficiently explores holistic characteristics
 496 and interrelated changes among the different frames in the same subject
 497 to directly analyze LV sequence and LV biological structure for adaptively
 498 learning all cardiac indices. And U-net (Ronneberger et al., 2015) just
 499 automatically provides LV area from its segmentation while the other indices
 500 need extra interaction from the expert for apex and mitral valve plane.

501 In the implementation of comparison, our proposed method needs no
 502 extra interaction. Our method is fed with entire echo image and does not
 503 require post-processing, benefited from its robust processing ability. But
 504 the other direct methods need to be performed on the the pre-handcrafted
 505 region to work (Zhen et al., 2014b, 2015a, 2016; Xue et al., 2017a). The
 506 segmentation method U-net is post processed as general with maximum
 507 connected region extraction to improve its segmentation results for indices
 508 estimation.

509 5.6. Performance of Activation Function and Hyper Parameters Selection

510 **Activation Function ELU vs. ReLU.** As shown in Figure. 12,
 511 ELU better fits the RRU than ReLU, with the lower estimation MAE
 512 (sum of normalized multitype indices MAE). Since the activation of ELU
 513 is able to transmit not only positive value message but also negative value
 514 message among frames, which is important for stimulating the inter-frames
 515 communication. But ReLU misses the information during the negative
 516 regime because of all being forcefully pushed to zero.

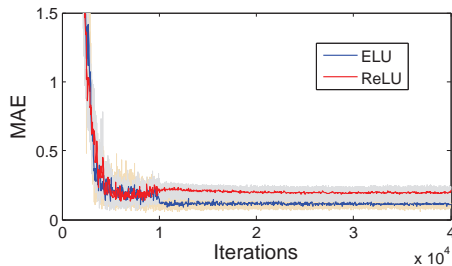


Figure 12: ELU activation outperforms ReLU in the RRU with lower testing MAE and better fitting.

517 **Hyper Parameters Setting.** As shown in Figure. 13, our Hyper
 518 parameters of $\lambda_1 = 1000$, $\lambda_2 = 1$ and $\lambda_3 = 0.1$ gain the best estimation
 519 accuracy compared to the other settings, with the lowest estimation MAE.
 520 Defaulting λ_2 for indices estimation as 1, λ_1 gets the large magnitude of 1000
 521 for the trade-off between the trainable tasks location and indices estimation
 522 to mutually promote them; λ_3 with the small magnitude of 0.1 balances tasks
 523 training and network parameters regularization. Figure 13(a) indicates that
 524 the large λ_1 is more effective than small setting as larger ones have lower
 525 rate of accuracy decay. Specifically, λ_1 setting smaller than 1000 extremely
 526 increases the estimation error. Since the unsuitable small λ_1 decreases the
 527 location supervision of LV-ROI, which leads the indices estimation in a mess.
 528 The messed indices estimation then arbitrarily misleads the location through
 529 the joint learning and further degrades the indices accuracy in return via the
 530 chain reaction. Big is better, but not infinite. The too huge magnitude of λ_1
 531 exceeding 1000 also has the risk of decreasing the performance. Because the
 532 too huge λ_1 weakens the effect of indices estimation in the mutual promotion,
 533 so that make the indices accuracy lower. In Figure 13(b), our choice also gets
 534 the best result. The big λ_3 , as 1 and 10, have the serious problem of making
 535 the learning target unclear, so that influence the learning ability. Small λ_3
 536 keeps the learning target clear, but the too tiny λ_3 of 0.01 and 0.001 weakens
 537 the regularization on network parameters so that reduces the generalization
 538 of the network and worsens the practical estimation.

539 6. Conclusions

540 In this paper, we proposed the PV-LVNet for the first time achieve the
 541 direct and accurate estimation of LV multitype indices (LAD_{A2C} , SAD_{A2C} ,
 542 $Area_{A2C}$, LAD_{A4C} , SAD_{A4C} , $Area_{A4C}$, $Volume$) from 2D echos of paired
 543 apical views. The PV-LVNet conducts the sufficient metrics from various
 544 dimensions (1D, 2D & 3D) and views (A2C, A4C, and union of A2C+A4C)

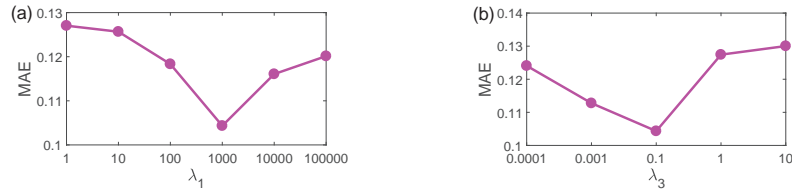


Figure 13: Our hyper-parameters setting gets the best estimation accuracy. (a) Influence of λ_1 selection. (b) Influence of λ_3 selection.

545 to provide a reliable comprehensive cardiac function assessment. It is
 546 built based on the Res-circle Net for sequential analysis. The Res-circle
 547 Net embeds both subject holistic characteristics and temporal changes
 548 by combining common subject-level base among frames and interrelated
 549 residuals of each frame, so that accurate and consistent location and indices
 550 estimation of LVs in echo sequence are enabled. The PV-LVNet is integrated
 551 of three interdependent parts for location, cropping and indices regression, as:
 552 1) the LV location module utilizes AED that gives different scaled metrics on
 553 different directions as the loss to suit approximate bullet shape of LV in apical
 554 echos, so that robust and efficient location for indices estimation is ensured;
 555 2) the Image Resampling automatically crops LV-ROI from the entire echo
 556 image, so that the interference of various structures in paired views is
 557 reduced; 3) by using inter-frames gradient regularization for exploring indices
 558 inter-frame relatedness, the LV location module fits not only each index value
 559 but also the indices evolution, so that sequential indices estimation is further
 560 enhanced. The PV-LVNet reaches high accuracy on all indices estimation and
 561 maintains excellent internal consistency with the ground truth, indicating its
 562 great potential in clinical cardiac function evaluation.

563 Acknowledgment

564 This work was supported by the Postgraduate Research & Practice
 565 Innovation Program of Jiangsu Province (No. KYCX17_0104); the China
 566 Scholarship Council (No. 201706090248); the States Key Project of Research
 567 and Development Plan (No. 2017YFA0104302, 2017YFC0109202 and
 568 2017YFC0107900); the National Natural Science Foundation (No. 81530060
 569 and 61871117); and the Science and Technology Program of Guangdong (No.
 570 2018B030333001).

571 References

572 Abdi, A.H., Luong, C., Tsang, T., Allan, G., Nouranian, S., Jue, J., Hawley,
 573 D., et al., 2017. Automatic quality assessment of echocardiograms using

- 574 convolutional neural networks: Feasibility on the apical four-chamber view.
575 IEEE Transactions on Medical Imaging 36, 1221–1230.
- 576 Afshin, M., Ayed, I.B., Islam, A., et al., 2012. Global assessment of cardiac
577 function using image statistics in mri, in: MICCAI, Springer. pp. 535–543.
- 578 Afshin, M., Ayed, I.B., Punithakumar, K., Law, M.W., et al., 2014. Regional
579 assessment of cardiac left ventricular myocardial function via mri statistical
580 features. IEEE Transactions on Medical Imaging 33, 481–494.
- 581 Ba, J., Kiros, J., Hinton, G., 2016. Layer normalization. arXiv preprint
582 arXiv:1607.06450 .
- 583 Carneiro, G., Nascimento, J.C., Freitas, A., 2012. The segmentation of
584 the left ventricle of the heart from ultrasound data using deep learning
585 architectures and derivative-based search methods. IEEE Transactions on
586 Image Processing 21, 968–982.
- 587 Chen, H., Zheng, Y., Park, J.H., Heng, P.A., et al., 2016. Iterative multi-
588 domain regularized deep learning for anatomical structure detection and
589 segmentation from ultrasound images, in: MICCAI, Springer. pp. 487–495.
- 590 Ciampi, Q., Villari, B., 2007. Role of echocardiography in diagnosis and
591 risk stratification in heart failure with left ventricular systolic dysfunction.
592 Cardiovascular Ultrasound 5, 1–12.
- 593 Clevert, D.A., et al., 2015. Fast and accurate deep network learning by
594 exponential linear units (elus). arXiv preprint arXiv:1511.07289 .
- 595 Cronbach, L.J., 1951. Coefficient alpha and the internal structure of tests.
596 psychometrika 16, 297–334.
- 597 Dai, J., He, K., Sun, J., 2016. Instance-aware semantic segmentation via
598 multi-task network cascades, in: CVPR, pp. 3150–3158.
- 599 Debreuve, E., Barlaud, M., Aubert, G., Laurette, I., et al., 2001. Space-time
600 segmentation using level set active contours applied to myocardial gated
601 spect. IEEE Transactions on Medical Imaging 20, 643–659.
- 602 Gao, Z., Li, Y., Sun, Y., Yang, J., Xiong, H., et al., 2018. Motion tracking
603 of the carotid artery wall from ultrasound image sequences: a nonlinear
604 state-space approach. IEEE Transactions on Medical Imaging 37, 273–283.

- 605 Gao, Z., Xiong, H., Liu, X., Zhang, H., Ghista, D., Wu, W., Li, S., 2017.
606 Robust estimation of carotid artery wall motion using the elasticity-based
607 state-space approach. *Medical Image Analysis* 37, 1–21.
- 608 Georgescu, B., Zhou, X.S., et al., 2005. Database-guided segmentation of
609 anatomical structures with complex appearance, in: *CVPR*, pp. 429–436.
- 610 Graves, A., 2012. Supervised sequence labelling, in: *Supervised sequence*
611 *labelling with recurrent neural networks*. Springer, pp. 5–13.
- 612 He, K., Zhang, X., Ren, S., Sun, J., 2016a. Deep residual learning for image
613 recognition, in: *CVPR*, pp. 770–778.
- 614 He, K., Zhang, X., et al., 2016b. Identity mappings in deep residual networks,
615 in: *European conference on computer vision*, Springer. pp. 630–645.
- 616 Jacob, G., Noble, J.A., Behrenbruch, C., Kelion, A.D., Banning, A.P.,
617 2002. A shape-space-based approach to tracking myocardial borders and
618 quantifying regional left-ventricular function applied in echocardiography.
619 *IEEE Transactions on Medical Imaging* 21, 226–238.
- 620 Jaderberg, M., Simonyan, K., et al., 2015. Spatial transformer networks, in:
621 *Advances in neural information processing systems*, pp. 2017–2025.
- 622 Lang, R.M., Badano, L.P., Mor-Avi, V., Afilalo, J., Armstrong, A., Ernande,
623 L., Flachskampf, F.A., et al., 2015. Recommendations for cardiac chamber
624 quantification by echocardiography in adults: an update from the american
625 society of echocardiography and the european association of cardiovascular
626 imaging. *Journal of the American Society of Echocardiography* 28, 1–39.
- 627 Lang, R.M., Bierig, M., Devereux, R.B., Flachskampf, F.A., Foster, E.,
628 Pellikka, P.A., Picard, M.H., et al., 2006. Recommendations for chamber
629 quantification. *European Journal of Echocardiography* 7, 79–108.
- 630 Lathuilière, S., Juge, R., et al., 2017. Deep mixture of linear inverse
631 regressions applied to head-pose estimation, in: *CVPR*, pp. 4817–4828.
- 632 Luo, G., Dong, S., Wang, K., Zuo, W., Cao, S., Zhang, H., 2018. Multi-views
633 fusion cnn for left ventricular volumes estimation on cardiac mr images.
634 *IEEE Transactions on Biomedical Engineering* 65, 1924 – 1934.

- 635 Malladi, R., Sethian, J.A., Vemuri, B.C., 1995. Shape modeling with front
636 propagation: A level set approach. *IEEE Transactions on Pattern Analysis
637 and Machine Intelligence* 17, 158–175.
- 638 Mo, Y., Liu, F., McIlwraith, D., Yang, G., Zhang, J., He, T., Guo, Y., 2018.
639 The deep poincaré map: A novel approach for left ventricle segmentation,
640 in: *MICCAI*, Springer. pp. 561–568.
- 641 Nascimento, J.C., et al., 2008. Robust shape tracking with multiple models in
642 ultrasound images. *IEEE Transactions on Image Processing* 17, 392–406.
- 643 Oktay, O., Ferrante, E., Kamnitsas, K., Heinrich, M., Bai, W., Caballero,
644 J., Cook, S.A., de Marvao, A., et al., 2018. Anatomically constrained
645 neural networks (acnns): application to cardiac image enhancement and
646 segmentation. *IEEE Transactions on Medical Imaging* 37, 384–395.
- 647 Paragios, N., 2003. A level set approach for shape-driven segmentation and
648 tracking of the left ventricle. *IEEE Transactions on Medical Imaging* 22,
649 773–776.
- 650 Pascual, M., Pascual, D., Soria, F., Vicente, T., Hernandez, A., Tebar, F.,
651 Valdes, M., 2003. Effects of isolated obesity on systolic and diastolic left
652 ventricular function. *Heart* 89, 1152–1156.
- 653 Peng, P., Lekadir, K., Gooya, A., et al., 2016. A review of heart chamber
654 segmentation for structural and functional analysis using cardiac magnetic
655 resonance imaging. *Magnetic Resonance Materials in Physics* 29, 155–195.
- 656 Pereira, S., et al., 2018. Enhancing interpretability of automatically extracted
657 machine learning features: application to a rbm-random forest system on
658 brain lesion segmentation. *Medical image analysis* 44, 228–244.
- 659 Ravi, D., Wong, C., Deligianni, F., et al., 2017. Deep learning for health
660 informatics. *IEEE Journal of Biomedical and Health Informatics* 21, 4–21.
- 661 Ronneberger, O., Fischer, P., Brox, T., 2015. U-net: Convolutional networks
662 for biomedical image segmentation, in: *MICCAI*, Springer. pp. 234–241.
- 663 Schiller, N.B., Shah, P.M., Crawford, M., DeMaria, A., Devereux, R.,
664 Feigenbaum, H., Gutgesell, H., Reichek, N., et al., 1989. Recommendations
665 for quantitation of the left ventricle by two-dimensional echocardiography.
666 *Journal of the American Society of Echocardiography* 2, 358–367.

- 667 Szegedy, C., Ioffe, S., et al., 2017. Inception-v4, inception-resnet and the
668 impact of residual connections on learning, in: AAAI, pp. 4278–4284.
- 669 Vigneault, D.M., Xie, W., Ho, C.Y., et al., 2018. ω -net (omega-net): Fully
670 automatic, multi-view cardiac mr detection, orientation, and segmentation
671 with deep neural networks. *Medical Image Analysis* 48, 95–106.
- 672 Wang, Z., Salah, M.B., Gu, B., Islam, A., Goela, A., Li, S., 2014. Direct
673 estimation of cardiac biventricular volumes with an adapted bayesian
674 formulation. *IEEE Transactions on Biomedical Engineering* 61, 1251–1260.
- 675 Wu, L., Cheng, J.Z., Li, S., Lei, B., Wang, T., Ni, D., 2017. Fuiqa: Fetal
676 ultrasound image quality assessment with deep convolutional networks.
677 *IEEE Transactions on Cybernetics* 47, 1336–1349.
- 678 Xingjian, S., Chen, Z., Wang, H., Yeung, D.Y., , et al., 2015. Convolutional
679 lstm network: A machine learning approach for precipitation nowcasting,
680 in: *Advances in neural information processing systems*, pp. 802–810.
- 681 Xu, C., Xu, L., Gao, Z., Zhao, S., Zhang, H., Zhang, Y., et al., 2018. Direct
682 delineation of myocardial infarction without contrast agents using a joint
683 motion feature learning architecture. *Medical image analysis* 50, 82–94.
- 684 Xue, W., Brahm, G., et al., 2018. Full left ventricle quantification via deep
685 multitask relationships learning. *Medical Image Analysis* 43, 54–65.
- 686 Xue, W., Islam, A., Bhaduri, M., Li, S., 2017a. Direct multitype cardiac
687 indices estimation via joint representation and regression learning. *IEEE*
688 *Transactions on Medical Imaging* 36, 2057–2067.
- 689 Xue, W., Lum, A., Mercado, A., Landis, M., et al., 2017b. Full quantification
690 of left ventricle via deep multitask learning network respecting intra-and
691 inter-task relatedness, in: *MICCAI*, Springer. pp. 276–284.
- 692 Xue, W., Nachum, I.B., Pandey, S., Warrington, J., Leung, S., Li, S., 2017c.
693 Direct estimation of regional wall thicknesses via residual recurrent neural
694 network, in: *IPMI*, Springer. pp. 505–516.
- 695 Yu, L., Yang, X., Chen, H., Qin, J., Heng, P.A., 2017. Volumetric convnets
696 with mixed residual connections for automated prostate segmentation from
697 3d mr images, in: AAAI, pp. 66–72.

- 698 Zhen, X., Islam, A., Bhaduri, M., Chan, I., Li, S., 2015a. Direct and
699 simultaneous four-chamber volume estimation by multi-output regression,
700 in: MICCAI, Springer. pp. 669–676.
- 701 Zhen, X., Wang, Z., Islam, A., Bhaduri, M., Chan, I., Li, S., 2016. Multi-
702 scale deep networks and regression forests for direct bi-ventricular volume
703 estimation. *Medical Image Analysis* 30, 120–129.
- 704 Zhen, X., Wang, Z., Islam, A., Chan, I., Li, S., 2014a. A comparative study
705 of methods for cardiac ventricular volume estimation, in: Annual Meeting-
706 Radiological Society of North America (RSNA), pp. 228–244.
- 707 Zhen, X., Wang, Z., Yu, M., Li, S., 2015b. Supervised descriptor learning
708 for multi-output regression, in: Proceedings of the IEEE conference on
709 computer vision and pattern recognition, pp. 1211–1218.
- 710 Zhen, X., Wang, Z., et al., 2014b. Direct estimation of cardiac bi-ventricular
711 volumes with regression forests, in: MICCAI, Springer. pp. 586–593.
- 712 Zhen, X., Yu, M., He, X., Li, S., 2017. Multi-target regression via robust
713 low-rank learning. *IEEE transactions on pattern analysis and machine
714 intelligence* 40, 497–504.

715 Conflicts of interest: none

Journal Pre-proof